Modeling of a Membrane Reactor System for Crude Palm Oil Transesterification. Part II: Transport Phenomena

Pin Pin Oh
Dept. of Chemical and Environmental Engineering, Faculty of Engineering, The University of Nottingham, Jalan Broga, 43500 Semenyih, Selangor, Malaysia

Engineering & Processing Research Division, Malaysian Palm Oil Board, Selangor, Malaysia

Mei Fong Chong
Dept. of Chemical and Environmental Engineering, Faculty of Engineering; Centre for Sustainable Palm Oil Research (CESPOR), The University of Nottingham, Jalan Broga, 43500 Semenyih, Selangor, Malaysia

Harrison Lik Nang Lau and Yuen May Choo
Engineering & Processing Research Division, Malaysian Palm Oil Board, Selangor, Malaysia

Junghui Chen
Dept. of Chemical Engineering, Chung-Yuan Christian University, Chung-Li, Taiwan 320, R.O.C.

DOI 10.1002/aic.14763
Published online March 7, 2015 in Wiley Online Library (wileyonlinelibrary.com)

The mechanistic modeling of biodiesel production process in membrane reactor with the consideration of chemical reaction, phase equilibrium, and ultrafiltration is important for the membrane reactor design. In part II of this work, the chemical and phase equilibrium (CPE) model for crude palm oil transesterification reaction in the membrane reactor developed in part I is extended to an integration of CPE with modified Maxwell–Stefan model, which considers multicomponent mass transport phenomena of concentration polarization and intramembrane. A good fit of simulated permeate fluxes and apparent solute rejection to the experimental data shows that the model has a good prediction capability. Reversible fouling was found to be the major fouling and no pore plugging was observed. Simulation results verified that micelles were retained by the membrane at CPO:MEOH molar ratio of 1:24 and catalyst concentration of 0.5 wt %. However, phase inversion happened when catalyst concentration of 0.05 and 0.1 wt % were used. © 2015 American Institute of Chemical Engineers *AIChE J*, 61: 1981–1996, 2015
Keywords: Maxwell–Stefan, mass transport phenomena, membrane reactor, transesterification, biodiesel

Introduction

For transesterification reaction in a 6-L membrane reactor, reaction occurs in a two-phase system, as oil and alcohol are immiscible. Nevertheless, heterogeneous reaction can occur at the micelle interface in the reactor. To consider every single solute in the mixture is in contact with the surrounding bulk liquid and can be described by the bulk composition, one relatively simple kinetic called "pseudohomogeneous" kinetic approach can be used. For such a two-phase reaction system, chemical reaction and phase equilibrium should always be computed simultaneously to consider their strong interaction. Thus, chemical and phase equilibrium (CPE) study was conducted and discussed in part I of this paper series.

As the scale size of membrane reactor developed in this study was 6 L, the biodiesel process in the membrane reactor was considered as a lab-scale process. Looking at the complexity of multiphase of the recycle loop operation as shown in Figure 1 of part I of this two-paper series, mechanistic modeling approach to describe the transport phenomena of multicomponent biodiesel process in the membrane reactor with the consideration of heterogeneity behavior and CPE is important for the membrane reactor design.[1,2] There are several mathematical models describing the transport phenomena of binary or multicomponent separation in the membrane system which include the models based on particle-liquid,[3–5] liquid–liquid,[6,7] and gaseous separation[8–12] processes. There is also an article describes mass transport owing to molecular diffusion and viscous flow, as well as an instantaneous reversible reaction inside a membrane reactor for catalytic gas–solid reactions.[13] However, these models are not suitable for the membrane reactor developed in the present work that involves reversible transesterification reaction and liquid–liquid phase separation.

The economics of membrane filtration processes are largely dependent on the permeate flux.[14–16] Permeate flux deterioration due to concentration polarization and membrane fouling are the two main phenomena that set a serious limitation in various membrane filtration processes, and

Correspondence concerning this article should be addressed to M. F. Chong at meifong.chong@nottingham.edu.my or J. Chen at jason@wavenet.cycu.edu.tw.

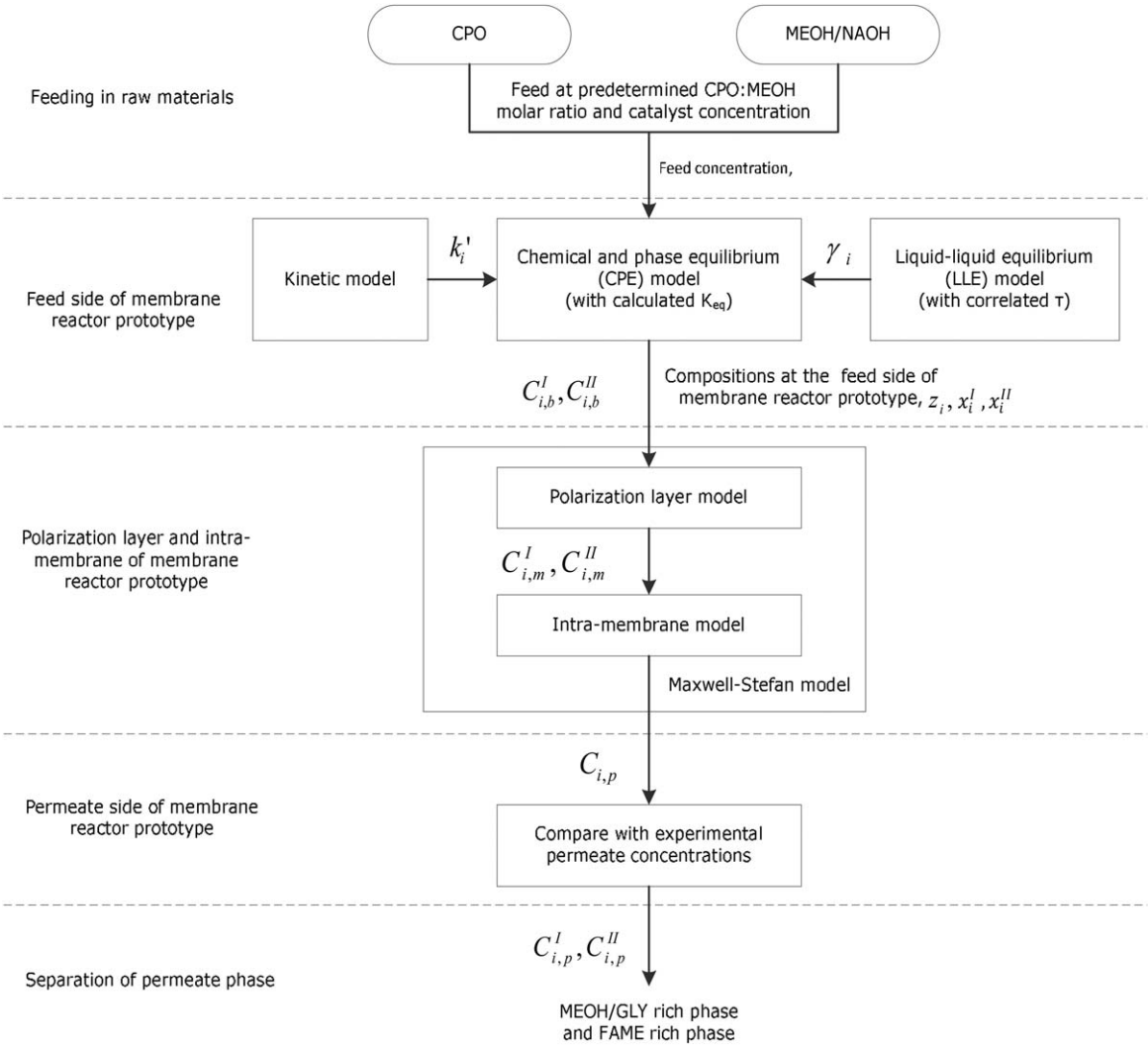

Figure 1. Overall flow diagram for the solution of Maxwell–Stefan model with the incorporation of CPE model.

affect the overall performance and economics.[17,18] Therefore, prediction on permeate flux deterioration based on different fouling mechanisms is the key investigation on the membrane performance.[19–22]

In ultrafiltration process, the fouling mechanisms can be attributed to concentration polarization on the membrane surface or surface fouling due to adsorption and gel-layer formation, and internal pore fouling due to pore adsorption and pore blocking.[17,23,24] Flux decline study in ultrafiltration process is commonly based on the boundary layer theory, which considers only the transport phenomena adjacent to the membrane surface.[25–27] Besides, the rejection of various components or solutes by an inert membrane is also an important factor in the ultrafiltration process. The membrane fouling is in close association with solute rejection because the membrane fouling could be caused by pore adsorption and pore blocking.[15,24,25,27–30]

Modeling of the permeate flux decline and solute separation in ultrafiltration process requires the consideration of two coupled transport phenomena caused by the concentration polarization in the boundary layer near the membrane surface and inside the membrane.[1,25] Rejection of solutes causes the accumulation of those particles in a thin layer adjacent to the membrane surface. The thin layer is often referred as polarization layer, and this phenomenon is called as concentration polarization. The extent of concentration polarization can be determined by the convection–diffusion equation, which combines the convective transport of particles toward the membrane and the diffusion of particles away from the membrane back into the bulk solution. Conversely, particles deposit onto the membrane surface or into the membrane pore surface may also influence the permeate flux, and it is often referred as membrane fouling.

Modeling of the mass transport phenomena at the membrane surface and inside the pores aids the understanding of macroscopic behavior in membrane separation, and provides estimates of the transport parameters and separation characteristics of the membrane.[25] For these reasons, the second part of this paper series focuses on the development of an ultrafiltration model for convective mass transport toward the membrane and permeation through a chemically inert porous membrane.

In the present article, a systematic model for the crude palm oil (CPO) transesterification in a membrane reactor for biodiesel production is developed for the first time by integrating the CPE model and the modified Maxwell–Stefan

Table 1. Order of Solute *i* and Solvent in MEOH-Rich Phase (Phase I) and TG-Rich Phase (Phase II)

i	Component in Phase I	Component in Phase II
1	Micelles	–
2	TG	TG
3	DG	DG
4	MG	MG
5	GLY	GLY
6	FAME	FAME
7	MEOH	MEOH

model. The integration of both models involves a few major steps as shown in Figure 1. The multicomponent bulk concentrations for each phase ($c^{\mathrm{I}}_{i,b}, c^{\mathrm{II}}_{i,b}$) at the feed side of the membrane can be estimated using the CPE model as presented in part I of this paper series. Subscript *b* represents the bulk phase. z_i is the component mole fraction in bulk phase, x^{I}_i and x^{II}_i are the component mole fraction in Phase I and Phase II, respectively. As the calculation of CPE model requires the effective rate constant, k'_i and activity coefficient, γ_i, both parameters can be estimated using kinetic model and thermodynamic model, respectively, from our previous work.[31,32]

Once the concentration of $c^{\mathrm{I}}_{i,b}$ and $c^{\mathrm{II}}_{i,b}$ are estimated, the permeation of MEOH-rich phase containing FAME through the membrane by retaining the TG-rich phase (micelle in this case) can be predicted using the modified Maxwell–Stefan model. The modified Maxwell–Stefan model considers the solutes and solvent mass transport phenomena at the membrane surface (polarization layer) and through the membrane (intramembrane). Once the permeate concentrations, $c_{i,p}$ are obtained, permeate phase separation into FAME-rich phase and MEOH/GLY-rich phase, at room temperature (298.15 K) can be estimated from the experimental data.

Model Development

Modified Maxwell–Stefan model

In a multicomponent system, there are two main kinds of forces need to take into account. They are the driving forces and friction forces, and the balance between them formed the generalized Maxwell–Stefan equation[33–36]

$$\sum_{\substack{j=1\\ j\neq i}}^{n}\frac{x_iN_j-x_jN_i}{c_t\text{Đ}_{ij}}=\frac{x_j}{RT}\nabla_{T,P}\mu_i+\frac{(\phi_i-\omega_i)}{c_tRT}\nabla P+\frac{x_iZ_iF}{RT}\nabla\Phi-\frac{\rho_i}{c_tRT}\left[g_i-\sum_{j=}^{n}\omega_jg_j\right] \tag{1}$$

In the present system, MEOH is regarded as solvent and other components are regarded as solutes. It consists of *n* solutes in a solvent with the order of solutes *i* and solvent as defined in Table 1.

In the present work, a heterogeneous system of multicomponent fluid mixture flows through an inert membrane with the assumptions made as follow,

1. The membrane is considered as a separate component, which does not influence the local thermodynamic and transport properties of the fluid, but which exerts a friction force on the fluid components.

2. The chemical potential gradient and the pressure gradient are the only important driving forces, while the electrical potential and other external body forces are negligible.

3. The mass transport is considered as one-dimension case.

4. The specific molar velocity of the membrane is equal to zero because it is mechanically constraint by the clamping force to keep the membrane in place.

5. The fluid behaves as continuum for which the molecular mean free path is much shorter than the pore diameter. In other word, both the diameters and the spacing of the intrapore molecules are short compared to the pore dimensions. Here, the generalized Maxwell–Stefan equations for multicomponent diffusion can be used.

6. Porosity and tortuosity corrections were included to relate the fluxes inside the membrane to the experimentally measurable fluxes outside the membrane.

In the present article, the multicomponent mass transport model was developed based on the modified Maxwell–Stefan model by Kerkhof.[1] The model is made up of a multicomponent boundary layer/concentration polarization model and an intramembrane model. The concentration polarization model is developed with the Vieth approximation for the turbulent diffusivity.[1] The model is about a more precise modeling of separate contributions of turbulence and diffusion by considering the thermodynamic effects and solute interactions in the polarization layer. For the intramembrane model, Kerkhof[1] had modified the generalized Maxwell–Stefan equations (Eq. 1), and referred to it as binary friction model. It considers both the friction forces caused by intermolecular diffusion and component-wall interaction. In this work, only the mass transport in radial direction that is normal to the direction of flow in the tubular membrane reactor was considered, and assumed that the effect of axial mass transport in negligible.

Mass transfer inside the membrane

When the membrane is introduced as a separate component into the multicomponent mixture system, the friction exerted by the membrane is included in Eq. 1 as a separate component. The number of solute in the fluid is denoted as *n* and the membrane is denoted as *m* in subscript. As the flux of the membrane (N_m) is equal to zero, Eq. 1 is then becomes

$$\sum_{\substack{j=1\\ j\neq i}}^{n}\frac{x_iN_j-x_jN_i}{c_t\text{Đ}_{ij}}-r_{im}N_i=\frac{x_j}{RT}\nabla_{T,P}\mu_i+\frac{\phi_i}{c_tRT}\nabla P \tag{2}$$

in which

$$r_{im}N_i=\alpha_m\kappa_i\phi_iu_i \tag{3}$$

where r_{im} is the friction force between the solute *i* and membrane, *m*. α_m is the membrane resistance factor and κ_i is the fractional viscosity coefficient. α_m is considered as depending only on the membrane structure, it then becomes

$$\alpha_m=\frac{1}{B_o} \tag{4}$$

where B_o is permeability parameter. Substituting Eqs. 3 and 4 into Eq. 2 gives[1]

$$\sum_{\substack{j=1\\ j\neq i}}^{n}\frac{x_iN_j-x_jN_i}{c_t\text{Đ}_{ij}}-\frac{1}{B_o}\kappa_i\phi_iu_i=\frac{x_j}{RT}\nabla_{T,P}\mu_i+\frac{\phi_i}{c_tRT}\nabla P \quad (5)$$

in which the binary Maxwell–Stefan diffusion coefficients are equal[34]

$$\text{Đ}_{ij}=\text{Đ}_{ji} \quad (6)$$

Equation 5 is then arranged into friction matrices by following the derivation adopted from Kerkhof[1] as presented in Appendix. Equation 5 becomes

$$(N_m)=-[G']^{-1}[\Gamma_c]\frac{\partial(c'_i)}{\partial z}+u^v\left[G'\right]^{-1}[F'](c'_i) \quad (7)$$

where N_m are the fluxes inside the membrane per unit of pore area with the friction matrices, $\left[G'\right]_{ij}$, $[B]_{ii}$, $[B]_{ij}$, $\left[F'\right]_{ij}$ are given as

$$\left[G'\right]_{ij}=\frac{\tau}{\varepsilon}\left\{[B]_{ij}+\delta_{ij}\frac{\kappa_ic_t\overline{V_i}}{B_o}-\frac{c_t^2x_i\overline{V_i}}{B_o}(\kappa_j\overline{V_j}-\kappa_n\overline{V_n})\right\} \quad (8)$$

$$[B]_{ii}=\frac{x_i}{\text{Đ}_{\text{in}}}+\sum_{\substack{k=1\\ k\neq i}}^{n}\frac{x_k}{\text{Đ}_{ik}} \quad (9)$$

$$[B]_{ij}=-x_i\left(\frac{1}{\text{Đ}_{ij}}+\frac{1}{\text{Đ}_{in}}\right)\qquad i\neq j \quad (10)$$

$$\left[F'\right]_{ij}=\frac{\tau}{\varepsilon}\left\{\delta_{ij}\left[\frac{c_t^2\overline{V_i}\cdot\overline{V_n}}{B_o}\kappa_n+\frac{1}{\text{Đ}_{in}}\right]\right\} \quad (11)$$

where δ_{ij} is the Kronecker delta, ε is the porosity, τ is the tortuosity, $\bar{V}$ is the specific molar volume. $[G']$ is the generalized friction matrix, $[B]$ is the Maxwell–Stefan friction matrix, and $[F']$ is the matrix in convection part of transport equation.

Analysis of a two-phase system requires modification of the thermodynamic correction factor matrix $[\Gamma_c]_{ij}$ to portray the nonideal behavior and it can be written as

$$[\Gamma_c]_{ij}=\begin{cases}\delta_{ij}+c_i\dfrac{\partial\ln\overline{\gamma}_i^{II}}{\partial c_j}-\dfrac{c_i}{c_t}\left(1-\dfrac{\overline{V_j}}{\overline{V_n}}\right) & ; \quad i=1\\ \delta_{ij}+c_i\dfrac{\partial\ln\overline{\gamma}_i^{I}}{\partial c_j}-\dfrac{c_i}{c_t}\left(1-\dfrac{\overline{V_j}}{\overline{V_n}}\right) & ; \quad i\neq 1\end{cases} \quad (12)$$

where $\bar{\gamma}$ is the average activity coefficient.

According to Kerkhof,[1] the value of κ_i in the generalized friction matrix $\left[G'\right]$ and convective part matrix $[F']$ can be defined as

$$\sum_{i=1}^{n}\kappa_ix_i=\frac{\eta_m}{\Delta P_{\text{total}}} \quad (13)$$

where η_m is the dynamic viscosity of mixture and ΔP_{total} is the transmembrane pressure. To solve Eq. 13, the κ_i is estimated with method of Wilke[37]

$$\kappa_i=\frac{1}{\Delta P_{\text{total}}}\frac{\eta_ix_i}{\sum_{j=1}^{n}x_j\xi_{ij}} \quad (14)$$

and

$$\xi_{ij}=\frac{\left[1+\left(\frac{\eta_i}{\eta_j}\right)^{0.5}\left(\frac{M_j}{M_i}\right)^{0.25}\right]^2}{\left[8\left(1+\frac{M_i}{M_j}\right)\right]^{0.5}} \quad (15)$$

in which η_i is the pure solute viscosities, ξ_{ij} is the interaction parameter, and M is the solute molecular weight.

The permeability B_o of a cylindrical pore of radius r_{pore} is defined as[38]

$$B_o=\frac{r_{\text{pore}}^2}{8} \quad (16)$$

In case of the solutes are only partially excluded from the membrane, the volume flux or volume-averaged velocity u^v can be calculated based on the equation as follow

$$u^v=L_p[\Delta P_{\text{total}}-\sigma\Delta\Pi] \quad (17)$$

where σ is the osmotic reflection coefficient, L_p is the hydraulic permeability, and $\Delta\Pi$ is the osmotic pressure difference.

The value of the osmotic reflection coefficient can be determined experimentally by either two methods[39] as follow

$$\sigma=\left[-\frac{u^v}{L_p\Delta\Pi}\right]_{\Delta P_{\text{total}}=0}=\left[\frac{\Delta P_{\text{total}}}{\Delta\Pi}\right]_{u^v=0} \quad (18)$$

The osmotic pressure different across the membrane, which depends on the concentration of both sides, is given as[1,5]

$$\begin{aligned}\Delta\Pi=RT\sum_{i=1}^{n}\frac{1}{\overline{\overline{V_i}}}\left(\ln\gamma_{\delta_{\text{pol}},i}+\ln c_{\delta_{\text{pol}},i}-\ln c_{\delta_{\text{pol}},t}\right)\\ -\frac{1}{\overline{\overline{V_i}}}(\ln\gamma_{p,i}+\ln c_{p,i}-\ln c_{p,t})\end{aligned} \quad (19)$$

in which

$$\gamma_{\delta_{\text{pol}},i}=\begin{cases}\bar{\gamma}^{II}_{\delta_{\text{pol}},i} & ; \quad i=1\\ \bar{\gamma}^{I}_{\delta_{\text{pol}},i} & ; \quad i\neq 1\end{cases};\quad \gamma_{p,i}=\begin{cases}\bar{\gamma}^{II}_{p,i} & ; \quad i=1\\ \bar{\gamma}^{I}_{p,i} & ; \quad i\neq 1\end{cases} \quad (20)$$

Symbol of γ denotes the activity coefficient. Subscript δ_{pol} and p represent the polarization-membrane interface and the permeate side, respectively.

To estimate the binary Maxwell–Stefan diffusion in a multicomponent system, the derivation from Taylor and Krishna[36] was adopted as

$$\text{Đ}_{ij}=\left(\text{Đ}^o_{ij}\right)^{\frac{1+x_j-x_i}{2}}\left(\text{Đ}^o_{ji}\right)^{\frac{1+x_i-x_j}{2}} \quad (21)$$

Wilke and Chang[40] correlation was used to estimate the diffusion coefficients in dilute liquid mixture

$$\text{Đ}^o_{ij}=7.4\times10^{-8}\frac{\left(\phi_jM_j\right)^{0.5}T}{\eta_jV_i^{0.6}} \quad (22)$$

where Đ^o_{ij} is the diffusion coefficient of solute i present in infinitely low concentration in solvent j, M_j is the molar mass of the solvent, T is temperature (K), η is the dynamic viscosity, and V_i is the molar volume of solute i at its normal boiling temperature. The association factor ϕ_j for the

solvent is equal to 1.9 for MEOH and 1.0 for other nonassociated solvents.

Mass transfer in the polarization layer

The mass balance of a solute at the membrane surface at steady-state condition gives the rate of convective transport of solute toward the membrane surface equal to the rate of solute permeate through the membrane plus the rate of solute due to back-diffusion.[41] In the present study, turbulent diffusion effect is considered in the concentration polarization layer. Thus, for one-dimensional mass transport in the polarization layer, the flux per unit area of the membrane is derived as[36]

$$\left(N_{\text{pol}}\right) = -\left\{[D] + [D]_{\text{turb}}\right\} \frac{\partial (c_i)}{\partial z} + u^v (c_i) \tag{23}$$

where N are the fluxes per unit area of the membrane and subscript pol represents the polarization layer.

The Fickian molecular diffusion matrix is defined as

$$[D] = [B]^{-1} [\Gamma_c] \tag{24}$$

The diffusion caused by the turbulent eddies in the polarization layer[42] as presented in the turbulence diffusion matrix, $[D]_{\text{turb}}$ is defined as[43,44]

$$[D]_{\text{turb}} = D_{\text{turb}} [I] \tag{25}$$

where $[I]$ is the identity matrix and D_{turb} is the turbulent diffusivity coefficient.

In this study, Vieth approximation is taken as the basis for the boundary layer theory.[1] The turbulent diffusivity coefficient, D_{turb} can be estimated from the turbulent Schmidt number, Sc_{turb}[36] as

$$Sc_{\text{turb}} = \frac{v_{\text{turb}}}{D_{\text{turb}}} \approx 1 \tag{26}$$

and the turbulent kinematic viscosity, v_{turb} is taken into account by the Vieth correlation[1,36]

$$\frac{v_{\text{turb}}}{v} = c_{\text{Vieth}} \left(\frac{f}{2}\right)^{\frac{3}{2}} \left(y^+\right)^3 \tag{27}$$

in which the constant c_{Vieth} is equal to

$$c_{\text{Vieth}} = \left(\frac{2}{9}\pi\sqrt{3}\right)^3 = 1.768 \tag{28}$$

In the polarization layer, a dimensionless distance coordinate perpendicular to the membrane wall, y^+ of ≤ 5 was considered as having the sufficient distance for the development of the concentration profile within the boundary layer thickness of δ_{pol}[1,42]

The Fanning friction factor, f was derived based on its relationship with the friction head, h_f as

$$h_f = \frac{2 f u_t^2 L_{\text{tube}}}{g d_{\text{tube}}} \tag{29}$$

where u_t is the bulk flow velocity, L_{tube} is the length of tubular membrane, g is the gravitation constant, and d_{tube} is the diameter of tubular membrane. The friction head was related to the pressure loss due to friction, ΔP_{fric} that can be measured experimentally as

$$\Delta P_{\text{fric}} = \rho g h_f \tag{30}$$

where ρ is the density of the fluid. By substituting Eq. 29 into Eq. 30, we obtained

$$\Delta P_{\text{fric}} = \frac{2 f u_t^2 L_{\text{tube}} \rho}{d_{\text{tube}}} \tag{31}$$

from which the Fanning friction factor can be calculated. The bulk velocity along the membrane u_t, also known as cross flow velocity, is defined as

$$u_t = \frac{Q_F}{n_{\text{tube}} \frac{\pi}{4} d_{\text{tube}}^2} \tag{32}$$

in which Q_F is the volume feed flow rate.

Boundary condition

As there is a surface of discontinuity (phase interface) between the polarization layer and membrane, the numerical procedure requires continuity equations at appropriate boundary conditions. The continuity equation for component i for the concentration polarization and intramembrane can be obtained from differential material balance. A mole balance on solute i over a differential element of width, Δz and cross-sectional area, A_c, whereby no chemical reaction in z-direction as shown in Figure 2 at the steady-state condition, gives

$$\text{Molar Flow Rate In} - \text{Molar Flow Rate Out} + \text{Rate of Generation} = \text{Rate of Accummulation}$$

$$F_{iz}|_z - F_{iz}|_{z+\Delta z} + 0 = \frac{\partial c_i}{\partial t} \cdot A_c \cdot dz \tag{33}$$

Dividing the Eq. 33 by $-\Delta z$ and taking the limit as $\Delta z \to 0$, gives

$$\frac{1}{A_c} \cdot \frac{\partial F_{iz}}{\partial z} = \frac{\partial c_i}{\partial t} \tag{34}$$

The molar flow rate, F_{iz} can be expressed in terms of molar flux N_i and A_c as

$$F_{iz} = N_{iz} A_c \tag{35}$$

Divide Eq. 35 by A_c and substitute it into Eq. 34, to get

$$\frac{\partial N_{iz}}{\partial z} = \frac{\partial c_i(t, V)}{\partial t} \tag{36}$$

The steady-state behavior was considered in the multicomponent mass-transfer study. For the permeation in z-direction at steady state, the equations of continuity as Eq. 37 for the polarization layer and as Eq. 38 for the intramembrane are obtained by substituting the flux of Eqs. 7 and 23 into Eq. 36, respectively. Equation 37 for polarization layer and Eq. 38 for intramembrane reduced to

$$\frac{\partial}{\partial z}\left(-\left\{[D] + [D]_{\text{turb}}\right\} \frac{\partial (c_i)}{\partial z} + u^v (c_i)\right) = 0 \tag{37}$$

$$\frac{\partial}{\partial z}\left(-[G']^{-1} [\Gamma_c] \frac{\partial (c'_i)}{\partial z} + u^v [G']^{-1} [F'] (c'_i)\right) = 0 \tag{38}$$

To solve Eqs. 37 and 38, the boundary layers as shown in Figure 2 and the boundary conditions presented as Eqs. 39–41 are considered. The boundary conditions for the combined models of polarization layer (Eqs. 39 and 40) and intramembrane (Eqs. 40 and 41) for ultrafiltration are given as

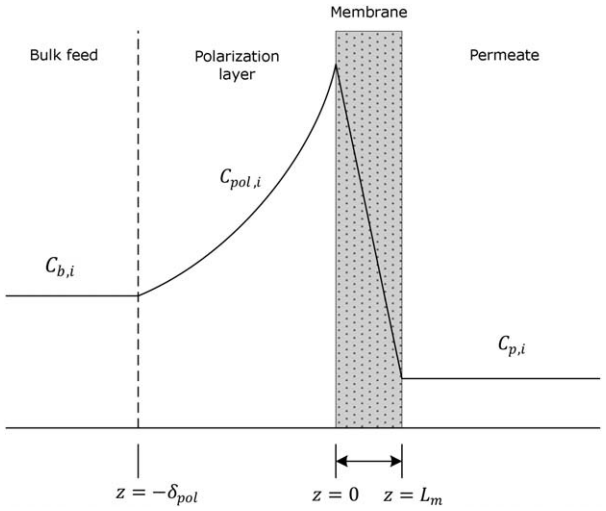

Figure 2. Schematic diagram of concentration polarization and intramembrane boundary layers.[45]

$$z=-\delta_{\text{pol}};\quad c_{i,-\delta_{\text{pol}}}=c_{i,b}\quad;\quad i=1,\ 2\ldots n \tag{39}$$

$$z=0;\quad c_i'=\begin{cases}\left[K_{\text{eq}}\right]^m c_{i,\text{pol}} & ;\quad i=1\\ \left[K_{\text{eq}}\right]^{\text{II}} c_{i,\text{pol}} & ;\quad i\neq 1\end{cases} \tag{40}$$

$$z=L_m;\quad c_i'=\left[K_{\text{eq}}\right]^m c_{i,p}\quad;\quad i=1,\ 2\ldots n \tag{41}$$

where $c_{i,-\delta_{\text{pol}}}$, $c_{i,b}$, $c_{i,\text{pol}}$, and $c_{i,p}$ are the solutes concentrations at bulk-polarization interface, bulk phase, polarization layer, and permeate phase, respectively. The parameter of δ_{pol} can be estimated from parameter estimation, which is discussed in the next section.

As shown in Figure 2, the $z=-\delta_{\text{pol}}$, $z=0$, and $z=L_m$ are the boundary set at the thickness of polarization layer, at the polarization layer-membrane interface, and the thickness of membrane, respectively. The $\left[K_{\text{eq}}\right]^{\text{II}}$ and $\left[K_{\text{eq}}\right]^m$ are equilibrium partition coefficients. $\left[K_{\text{eq}}\right]^{\text{II}}=\frac{\gamma^{\text{II}}}{\gamma^{\text{I}}}$ can be obtained from LLE thermodynamic model, and the only fitting parameter, $\left[K_{\text{eq}}\right]^m$ can be fitted from the mass transport model using the experimental data.

Parameter estimation

Hydraulic Permeability Constant, $\boldsymbol{L_p}$. The hydraulic permeability constant, L_p of Eq. 17 can be determined from the slope of the pure MEOH solvent flux, vs. the transmembrane pressure[46] based on Eq. 42. Pure MEOH solvent fluxes were obtained experimentally at various transmembrane pressures at room temperature and atmospheric pressure

$$u^v_{\text{MEOH}}=L_p\Delta P_{\text{total}} \tag{42}$$

The relationship between the transmembrane pressure and pure MEOH solvent flux, u^v_{MEOH} enables the determination of membrane resistance, R_m that was defined as

$$R_m=\frac{1}{L_p\eta_{\text{MEOH}}} \tag{43}$$

which is equivalent to[1,47]

$$R_m=\frac{L_m}{B_o}\frac{\tau}{\varepsilon} \tag{44}$$

Equation 44 can be used to calculate the ratio of $\frac{\tau}{\varepsilon}$.

Mass-Transfer Coefficient, $\boldsymbol{k}$. The mass-transfer coefficient, k, can be estimated using the correlation between the Sherwood number, Sh with Reynolds number, Re and Schmidt number, Sc, respectively, as[36]

$$Sh=0.023Re^{0.8}Sc^{0.33} \tag{45}$$

To solve Eq. 45, the Reynolds number, Re and Schmidt number can be calculated from Eqs. 46 and 47 as below

$$Re=\frac{\rho u_t d_{\text{tube}}}{\eta} \tag{46}$$

$$Sc=\frac{\eta}{\rho\bar{D}} \tag{47}$$

where d_{tube} is the diameter of tubular membrane tube, $\dot{\eta}$ is the dynamic viscosity of the fluid, and $\bar{D}$ is the average diffusive mass-transfer coefficient, which can be obtained by finding the mean value of $[D]$ calculated from Eq. 24.

After obtaining the Sherwood number, the mass-transfer coefficient, k can be calculated from Eq. 48

$$Sh=\frac{kd_{\text{tube}}}{\bar{D}} \tag{48}$$

Using the mass-transfer coefficient, k and average value for Fickian diffusive mass-transfer coefficient, $\bar{D}$, the polarization boundary layer thickness, δ_{pol} can be calculated from Eq. 49[48–50]

$$\delta_{\text{pol}}=\frac{\bar{D}}{k} \tag{49}$$

After obtaining δ_{pol}, it can be used to calculate the boundary conditions.

Modified Maxwell–Stefan model parameter estimation

$\left[K_{\text{eq}}\right]^m$ from the mass transport model is the only fitting parameter that requires minimizing a fit error function as shown in Figure 3. The experimental data for each of the components in the bulk solutions and permeate side at steady state were used in the model fitting to estimate the $\left[K_{\text{eq}}\right]^m$ value. The goodness of fit was measured by root mean squared deviation (RMSD), which defined as

$$\text{RMSD}=\left[\frac{1}{N}\sum_{i=1}^{N}\left(c_{i,p,\text{exp}}-c_{i,p,\text{calc}}\right)^2\right]^{0.5} \tag{50}$$

The iterating will stop when the RMSD value is within $\pm$ 5% as shown in Figure 3. The $R_{i,\text{app}}$ can be calculated by assuming Poiseuille flow in the pores as[51] as

$$R_{i,\text{app}}=1-\frac{c_{i,p}}{c_{i,b}} \tag{51}$$

The modified Maxwell–Stefan model was fitted with the experimental data using the genetic algorithm as the optimization tool of MATLAB.

Modified Maxwell–Stefan model solution

Once the bulk concentrations at the feed side of the membrane reactor, $c^{\text{I}}_{i,b}$ and $c^{\text{II}}_{i,b}$ obtained from the CPE calculation as discussed in part I of this article are known, the mass transport equations of polarization layer and intramembrane filtration can be solved by means of numerical procedure. As the procedure is iterative as shown in Figure 4, the initial

estimate of the rejection of each solute, $R_{i,\text{app,guess}}$ and u^v_{guess} are required.

The initial guess of $R_{i,\text{app,guess}}$ can be estimated from Eq. 51. The initial guess of u^v_{guess} can be estimated from the range of 0–1. Using the calculated values of the solute concentrations at the membrane-boundary layer interface ($z=0$) and at the membrane layer ($z=L_m$), $R_{i,\text{app,calc}}$ and u^v_{calc} are then calculated. The calculations of $R_{i,\text{app,calc}}$ and u^v_{calc} will be terminated when the error between the guess and the calculated values are less than 5% as shown in Figure 4.

Results and Discussion

Model regression and validation

Parameters required by the modified Maxwell–Stefan model integrated with CPE model developed in this work were obtained using literature and experimental data obtained from the CPO transesterification reaction using the membrane reactor. Experimental run 1, 4, and 7 as shown in Table 3 in part I in this paper series were used for parameter regression. The model prediction capability was then further validated by experimental runs of 2, 3, 5, 6, 8, and 9 at two different transmembrane pressures (TMPs) of 120.6 and 137.9 kPa.

The model parameters of thermodynamic factor, Γ_c, dynamic viscosities, and other physical properties of the reaction mixture were obtained from the UNIQUAC model and correlation based on literature data of Poling et al.[52] The values for the parameters of L_p and R_m were regressed from the pure permeability data of MEOH at the TMP range of 103.4–137.9 kPa. The values of the model parameters obtained in this study and its comparison with literature values are shown in Table 2.

The estimated value of L_p as shown in Table 2 was higher than the values reported by Mehta and Zydney[53] and Ahmad et al.[54] by a few order of magnitude. This observation with higher membrane permeability was expected as MEOH was used as the solvent, which is less viscous than water as reported by Viswanath et al.[55] Thus, MEOH permeated through the membrane at a higher rate than the water. This is reflected with a lower membrane resistance, R_m value measured as compared to the literature values.[53,54] The estimated value of reflection coefficient, σ as shown in Table 2 indicates that the membrane was selective toward solutes when solutes and MEOH solvent move across the membrane.[56]

Table 3 tabulates the diffusion coefficient of solutes in MEOH solvent obtained from the present work and literatures. It is noticed that the Maxwell–Stefan diffusion coefficients calculated in the present work were differed by partly two orders of magnitude with the literature values as reported by Stamenković et al.[58] and Portha et al.[57] This is quite reasonable considering that diffusion is the movement of individual molecules through the layer of molecules of the same substance (self-diffusion) or other substances (binary diffusion in which the molecules of two substances interdiffuse).[59] This shows that the diffusion coefficients obtained in the present work are acceptable to the study.

The values of $\left[K_{\text{eq}}\right]^{\text{II}}$ that represents the solubility of Phase I in the Phase II as tabulated in Table 4 were estimated from the CPE model calculation. Similar experimental runs were also used to regress the only fitting parameter $\left[K_{\text{eq}}\right]^m$ as tabulated in Table 4.

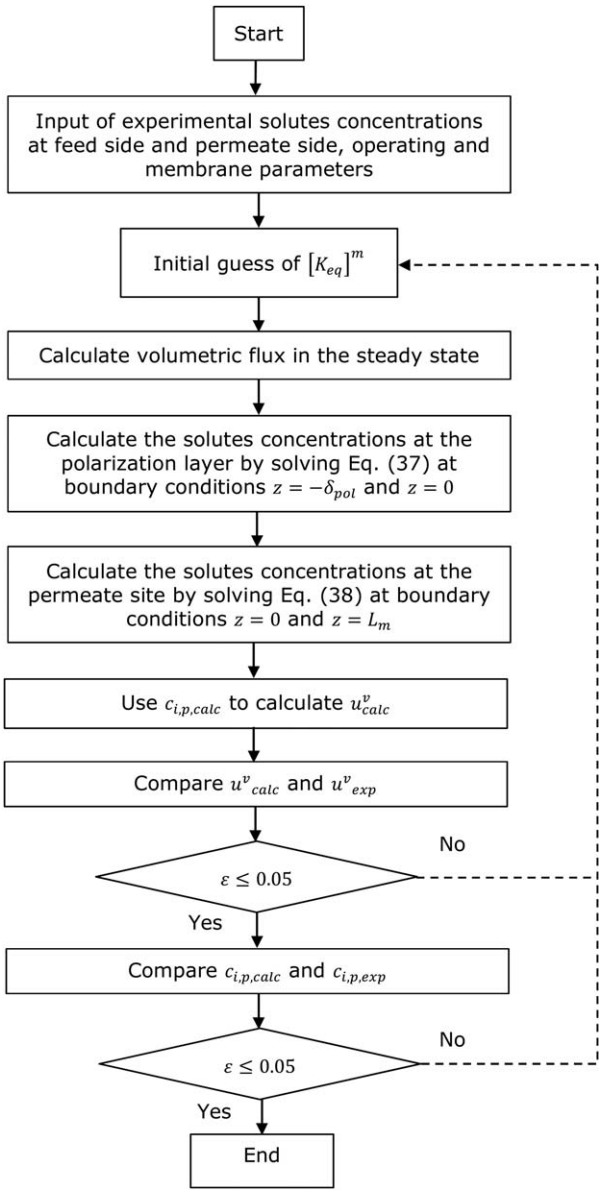

Figure 3. Flow diagram of the mass transport Maxwell–Stefan model fitting procedure.

The $\left[K_{\text{eq}}\right]^{\text{II}}$ values (as defined in Eq. 40) for the components of TG, DG, and MG were found to be lower than those of FAME, GLY, and MEOH as depicted in Table 4. By referring to the Eq. 11 in part I (as $\left[K_{\text{eq}}\right]^{\text{II}}=K_i=\frac{x_i^{\text{I}}}{x_i^{\text{II}}}$), this observation indicates that the components of TG, DG, and MG were more soluble in the Phase II than Phase I whereas the components of FAME, GLY, and MEOH were more soluble in the Phase I than Phase II. This phenomenon further confirmed the previous observations obtained based on Figure 6 in part I in which TG, DG, and MG were found to be more soluble in Phase II while FAME, GLY, and MEOH were more soluble in Phase I. These results further validated the equilibrium behavior of chemical and phase within the feed side of the membrane reactor. The observation also verified the assumption made in this study that the major resistance to permeation is governed by the solutes equilibrium with Phase II at the membrane surface rather than the membrane material itself as in Figure 2 in part I.

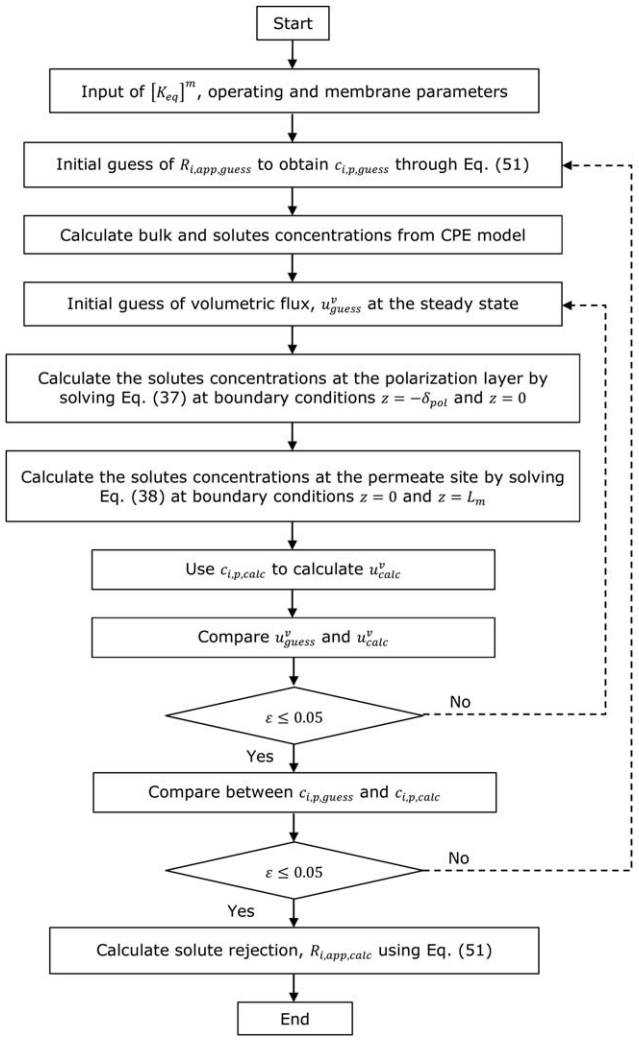

Figure 4. Flow diagram of the solution algorithm of the modified Maxwell–Stefan model.

The $[K_{eq}]^m$ defined in this study is to explain the partitioning relationship between solutes in the continuous phase and inert, porous membrane. By fitting the parameter of $[K_{eq}]^m$ with the experimental data, it was observed that $[K_{eq}]^m$ values tabulated in Table 4 decreased as the catalyst concentration increases. This indicates that solutes in the continuous phase are more soluble in the membrane than the concentration polarization layer as the catalyst concentration increases. Nevertheless, the $[K_{eq}]^m$ values of existing work was found slightly deviated from the $[K_{eq}]^m$ value of 0.69 obtained by Kerkhof[1] for the mass transport of PEG-3400 in an ultrafiltration system with tubular membrane module. The deviation of the $[K_{eq}]^m$ value can be related to the different solute and solvent involved in the ultrafiltration system as well as the membrane material used in the system.

The experimental permeate fluxes, apparent solute rejections, and model predicted results were depicted in Figures 5 and 6, respectively. The comparison between the simulated results and the experimental data at the TMP of 103.4 kPa for runs 1, 4, and 7 as shown in Figures 5 and 6 shows a good agreement with the error maintained within RMSD of $\pm 5\%$. This observations show that the parameter of $[K_{eq}]^m$ obtained using the global optimization method was satisfying.

Conversely, the model prediction of modified Maxwell–Stefan model integrated with CPE model was further validated by using independent sets of experimental runs. A good agreement between the experimental data and model predicted results were observed in all the experimental runs with the error values maintained within RMSD values ranges from 1.35 to 3.54% as shown in Figures 5 and 6. The good match between the model predicted results and experimental data shows that the integration of modified Maxwell–Stefan model and CPE model can be used to predict the permeate compositions, permeate fluxes, and solute rejections. It also proves the validity of the model that represents the CPO transesterification reaction and products separation in the membrane reactor.

Figure 5 illustrated the effect of TMP on the permeate flux of reaction mixture for UF ceramic membrane at steady state. In all cases, the permeate fluxes of reaction mixture were considered almost constant as the TMP increases. It is observed from Figure 5 that the permeate fluxes of reaction mixtures were lower than the permeate flux of pure MEOH solvent of $44.11 \times 10^{-7} \mathrm{m^3\ m^{-2}\ s^{-1}}$ at all the operating conditions of TMP and catalyst concentration. As the solutes of the reaction mixtures, which are the micelles in this case deposited onto the membrane surface to form a concentration polarization layer, reversible fouling adjacent to the membrane surface is found to be the major fouling phenomena of the membrane reactor. This can be further supported with the relatively constant permeate flux of reaction mixture with increasing TMP.

In addition, it is worth noting that the rejected solutes deposited on the membrane surface were removed completely by forward flushing with hot tap water and MEOH solvent after each experimental run. After each forward flushing, complete recovery of membrane permeability for MEOH solvent to the initial value of pure MEOH permeability was obtained. This observation is important as it proved that there was no adsorption or pore plugging of solutes in the membrane for reactions that were conducted under these operating conditions. Above all, these results show the validity of the model with the consideration of concentration polarization layer and intramembrane phenomena.

In Figure 6, the apparent solutes rejections, R_{app} were depicted as a function of TMP. The R_{app} values were found to be almost constant as the TMP increases, which correspond to the trend of flux vs. TMP as depicted in Figure 5. This observation shows that TMP does not affect the permeate flux and R_{app} in the present work. This observation is advantageous to the biodiesel production process using

Table 2. Estimated Parameters for the Modified Maxwell–Stefan Model

Parameter	Present Work	Literature	Reference
L_p ($\mathrm{m\ s^{-1}\ Pa^{-1}}$)	1.268 E −09[a]	2.500 E −10[b]	Mehta and Zydney[53]
		8.646 E −16[c]	Ahmad et al.[54]
R_m ($\mathrm{m^{-1}}$)	1.337 E +12	1.156 E +15	Mehta and Zydney[53]
		2.158 E +12	Ahmad et al.[54]
σ	0.8942	–	–

[a]Pure MEOH permeability in the ceramic membrane.
[b]Water permeability in the zirconium ceramic membrane.
[c]Water permeability in the ceramic membrane.

Table 3. Diffusion Coefficient of Solutes in MEOH Solvent

	$Đ_{i,MEOH}$ ($m^2\ s^{-1}$)						
Reference	Micelle	TG	DG	MG	GLY	FAME	MEOH
Present work[a]	N/A	1.21 E −11	1.10 E −11	1.14 E −11	4.29 E −11	7.60 E −10	1.38 E −07
Portha et al.[57b]	N/A	6.19 E −10	7.79 E −10	1.11 E −09	2.83 E −09	1.19 E −09	4.29 E −09
Stamenković et al.[58b]	N/A	7.80 E −10	N/A	N/A	N/A	N/A	N/A

[a]Maxwell–Stefan diffusion coefficients obtained in the present work.
[b]Diffusion coefficients obtained from the Wilke and Chang correlation.
N/A, Not applicable.

Table 4. The Regressed Parameters for Modified Maxwell–Stefan Model Using Experimental Data of Runs 1, 4, and 7

	$[K_{eq}]^{II}$							
NAOH (wt %)	TG	DG	MG	GLY	FAME	MEOH	$[K_{eq}]^{m}$	RMSD
0.05	5.50 E −09	2.62 E −03	1.48 E −03	3.89 E −01	1.77 E −02	1.50	0.9907	0.1523
0.1	1.53 E −09	1.11 E −01	3.01 E −03	4.15 E −01	6.31 E −02	1.53	0.7718	0.1835
0.5	8.42 E −03	8.44 E −05	4.61 E −02	5.47 E −01	2.54 E −02	1.60	0.2145	1.8029

membrane reactor, as operating the ultrafiltration membrane at low TMP requires low energy consumption.

Besides, it was observed that in Figures 6a, b high R_{app} values for micelles but low R_{app} values for TG solute were obtained for reactions that used catalyst concentration of 0.1 and 0.05 wt %, whereas high R_{app} values for TG, DG solutes, and micelles were obtained for reactions that used 0.5 wt % catalyst concentration. This indicates that TG permeated through the membrane when catalyst concentration of 0.05 and 0.1 wt % were used in the reaction at varying TMP. This observation indicates that catalyst concentration affects the final purity of biodiesel in membrane reactor. To have efficient product separation in the membrane reactor, it is important to operate the biodiesel production process at the appropriate catalyst concentration to control the CPE behavior of the reaction mixture. In this case, catalyst concentration of 0.5 wt % is needed if high R_{app} values for TG and micelles were desired.

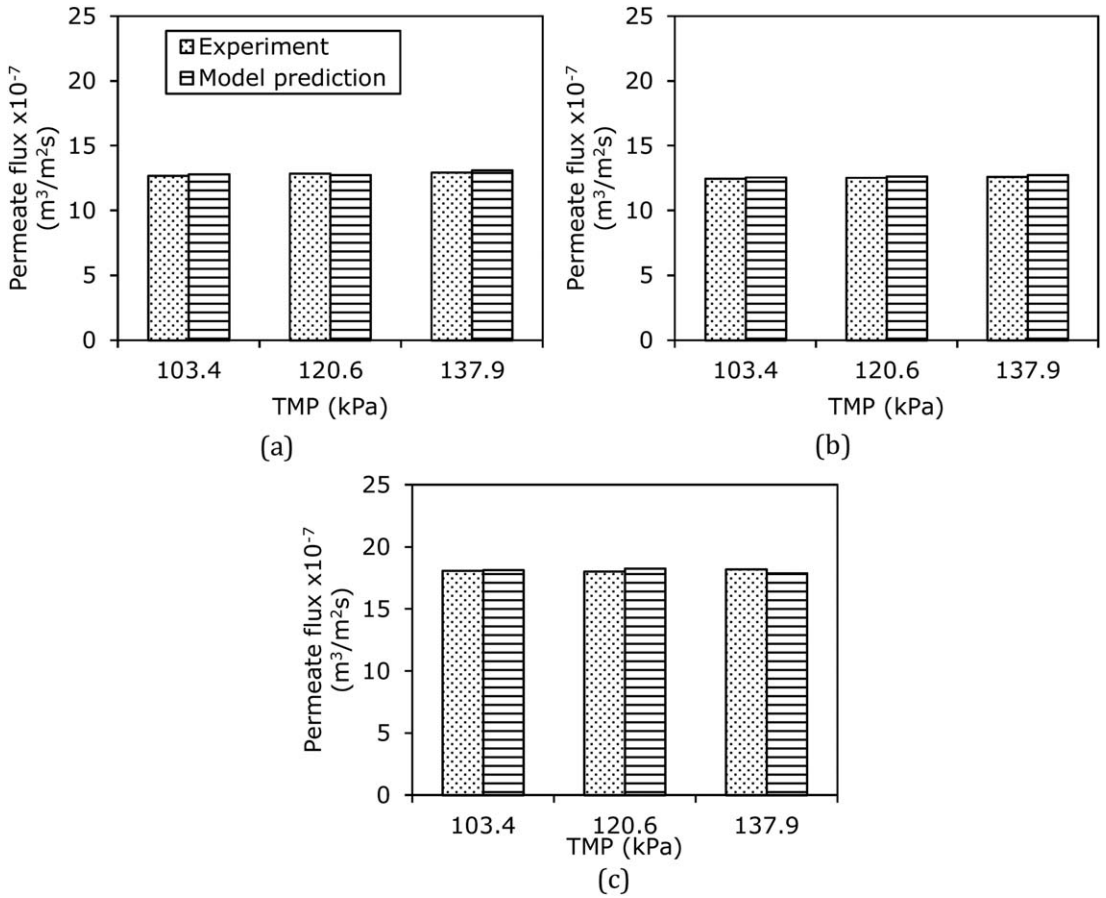

Figure 5. Experimental and simulation results of permeate flux at steady state as a function of TMP for reactions that used different catalyst concentration of (a) 0.05 wt %, (b) 0.1 wt %, and (c) 0.5 wt % with CPO:MEOH molar ratio of 1:24 at constant temperature of 333.15K.

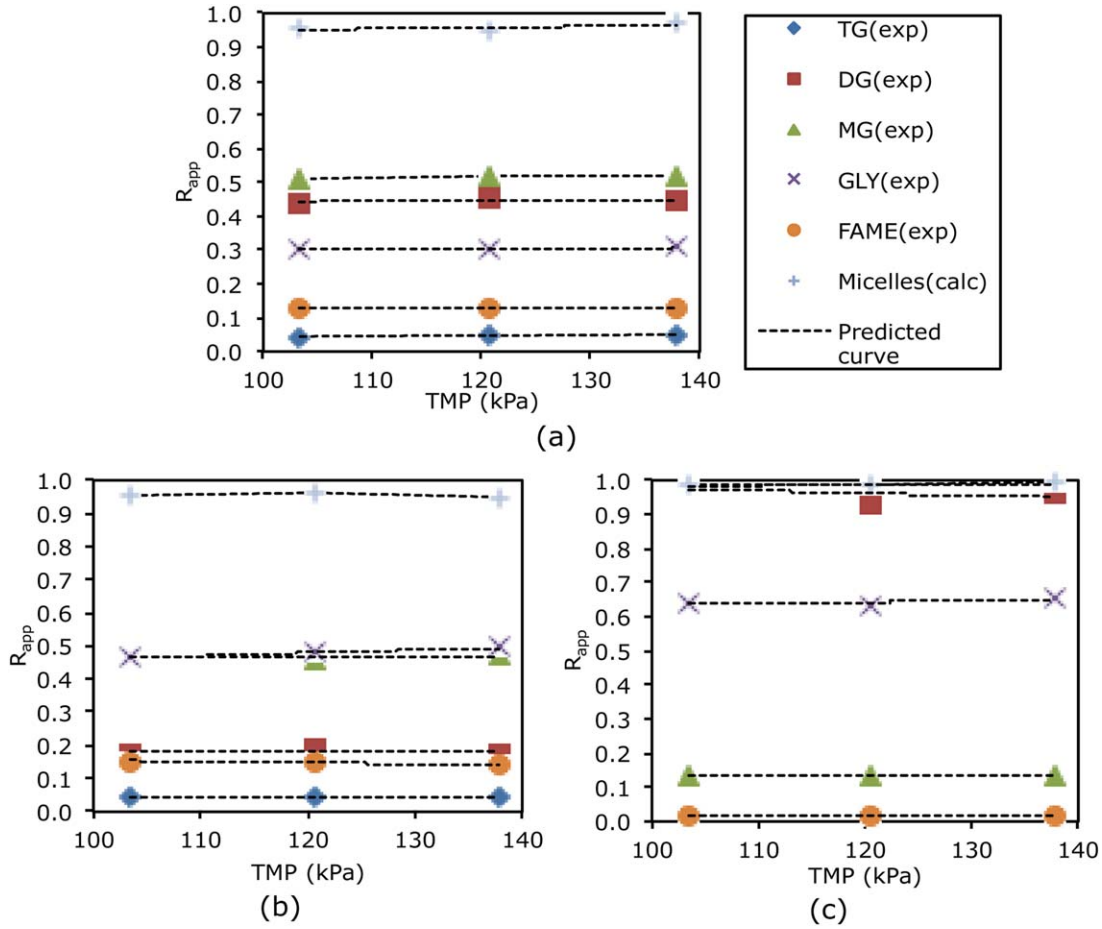

Figure 6. Experimental and simulation results of the apparent rejection for each solute as a function of TMP for reactions that used different catalyst concentration of (a) 0.05 wt %, (b) 0.1 wt %, and (c) 0.5 wt % with CPO:MEOH molar ratio of 1:24 at constant temperature of 333.15 K.

[Color figure can be viewed in the online issue, which is available at wileyonlinelibrary.com.]

Model evaluation

In this section, the developed model was used to evaluate the effects of CPE and mass transport behavior at the feed side of membrane reactor, concentration polarization and intramembrane on the final biodiesel purity in the membrane reactor. The comparisons of components compositions between the permeate stream (representing separation behavior) and micelles (representing CPE behavior) are shown in Figure 7.

A good agreement with the error maintained within RMSD of ±5% was observed in the comparison between the experimental data and predicted results as shown in Figure 7 for permeate stream compositions. The micelles in the emulsion at the feed side of the membrane reactor could not be measured, and therefore, only micelles concentrations simulated based on Eq. 52 were depicted in Figure 7

$$C^{I}_{\text{Micelle}} = C^{\text{II}}_{\text{TG}} + C^{\text{II}}_{\text{DG}} + C^{\text{II}}_{\text{MG}} + C^{\text{II}}_{\text{GLY}} + C^{\text{II}}_{\text{MEOH}} + C^{\text{II}}_{\text{FAME}} = \text{Phase II} \quad (52)$$

It is observable from Figure 7a that permeate is rich in MEOH while Figure 7b shows that micelles are rich in TG and FAME components for reaction that used catalyst concentration of 0.5 wt %. Interestingly, it is noticeable that Figures 7c, e show that permeate is rich in TG component while the micelles are rich in MEOH component as shown in Figures 7d, f for reaction that used catalyst concentration of 0.1 and 0.05 wt %. The observation in Figures 7c–f is contradicting with the one in Figures 7a, b. The underlying causes could be the effect of catalyst concentration toward the CPE of reaction mixture at the feed side of reactor.

To better understand the extent of current observation, Figure 7 presented in this article was compared with Figure 6 depicted in part I of this two-paper series. Figure 7a shows that the compositions of permeate obtained from membrane separation for both experiment and model simulation results were closely following the trend of compositions in Phase I obtained from CPE analysis at the feed side of the reactor as depicted in Figure 6a in part I.

Conversely, Figure 7b shows that the micelles compositions obtained from the model simulation are similar to the compositions of Phase II obtained from CPE at the feed side of the reactor as depicted in Figure 6b in part I. This indicates that a high rejection efficiency of micelles was achieved in the experimental run that used catalyst concentration of 0.5 wt % with CPO:MEOH molar ratio of 1:24 at temperature of 333.15 K and TMP of 103.4kPa.

This observation is consistent with results illustrated in Figure 6c that high R_{app} value for TG solute and micelles were obtained in the reaction that used catalyst concentration of 0.5 wt %. Thus, it is reasonable to find that TG solute and micelles were undetectable in Phase I and permeate stream, respectively, as illustrated in Figure 6a in part I and

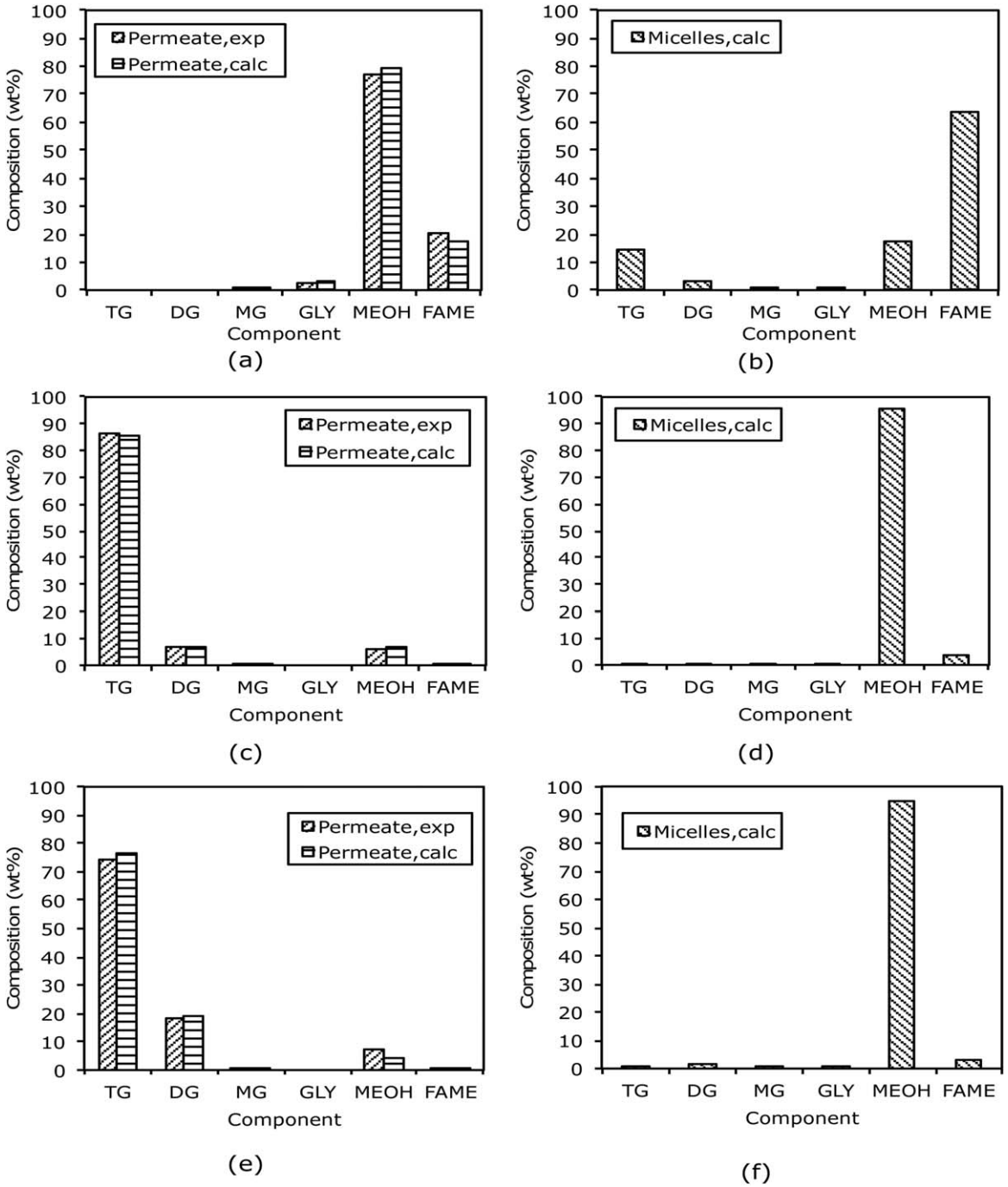

Figure 7. Permeate and micelles for reactions that used catalyst concentrations of 0.5 wt % (a, b), 0.1 wt % (c, d), and 0.05 wt % (e, f) with CPO:MEOH molar ratio of 1:24 at temperature of 333.15 K and TMP of 103.4 kPa.

Figure 7a in present article. These findings verified that micelles are formed by solutes in Phase II following to Eq. 52 and being retained by the membrane with high rejection. At the same time, the continuous phase (Phase I) permeated through the membrane. These observations verified the main assumption made in the model development.

Conversely, it is important to notice that the permeate compositions as depicted in Figures 7c, e were confirming with the compositions of Phase II obtained from CPE at the feed side of the reactor as depicted in Figures 6d, f in part I. The micelles compositions as depicted in Figure 7d, f were following the Phase I compositions obtained from CPE at the feed side of the reactor as depicted in Figures 6c, e in part I. This indicates that Phase II has become the continuous phase and permeates through the membrane while the membrane retained Phase I as micelles for reactions that used catalyst concentration of 0.05 and 0.1 wt % with CPO:MEOH molar ratio of 1:24 at temperature of 333.15 K and TMP of 103.4 kPa. Although two phases were obtained at the feed side of the reactor for all catalyst concentrations as illustrated in Figure 6 in part I, phase inversion had happen in such a way that Phase II or TG-rich phase becomes the continuous phase and permeated through the membrane as depicted in Figure 7.

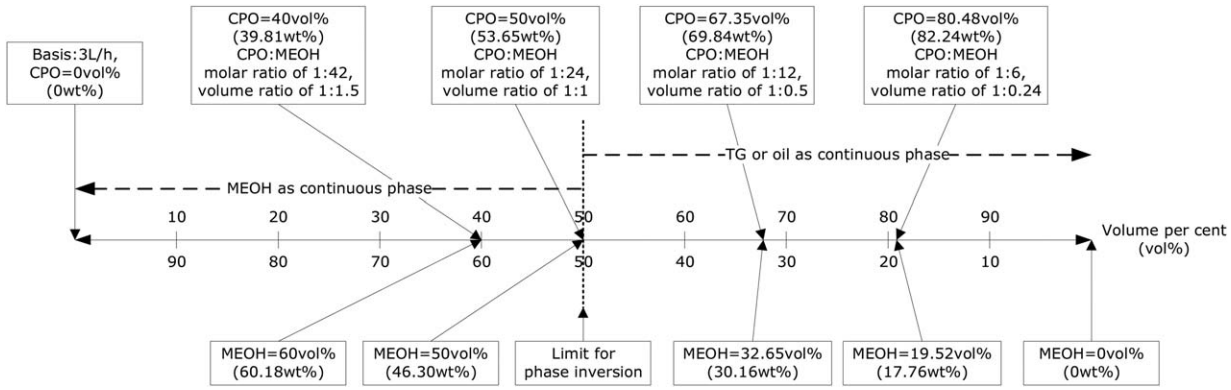

Figure 8. Scale of CPO and MEOH volume and mass percent at varying CPO:MEOH molar and volume percent ratios.

Furthermore, it is worth noting from Figures 8a, b in part I that TG compositions in the feed bulk phase fall into the range of 39–50 wt % where phase inversion happened in those reactions that used catalyst concentration of 0.05 and 0.1 wt %. Whereas Figure 7c in part I shows that TG compositions in the feed bulk phase fall into the range of 2–15 wt % for reaction that used catalyst concentration of 0.5 wt %, in which micelles were formed and TG free permeate was obtained. This finding was found consistent with the data reported by Cheng et al.[60] that oil-rich phase was rejected by the membrane when the feed bulk concentration is controlled within the two-phase zone with TG composition of 20 wt %. Above findings show that the rate of reaction needs to be controlled at a higher catalyst concentration so that TG composition in the feed bulk phase can be maintained within the two-phase zone with low concentration to prevent phase inversion.

In order further investigate the phase inversion behavior in the reaction; Figure 8 was used to analyze the feedstream conditions of the membrane reactor at varying CPO:MEOH molar ratios of 1:6, 1:12, 1:24, and 1:42. The phase behavior calculations of Eq. 4 in part I was conducted with the basis of 3 L of CPO. The CPO and MEOH in weight percent (wt %) corresponding to their respective volume percent (vol %) were also illustrated in Figure 8. As recommended by Falahati and Tremblay,[61] the amount of CPO (TG) at the feedstream of the reactor should not exceed the phase inversion limitation of 40–50 vol %, which is equivalent to 39.81–53.65 wt % as depicted in Figure 8, if the TG-rich phase need to be remained as the dispersed phase in the continuous MEOH-rich phase and separated by the membrane. Based on the illustration in Figure 8, the recommended CPO:MEOH molar ratio for biodiesel production in the membrane reactor would be at minimum of 1:24, in which the feedstream consists of CPO $\leq$ 53.65 wt % and MEOH $\geq$ 46.30 wt % whereby TG-rich micelles can be remained as dispersed phase in the continuous phase of MEOH. Phase inversion will happen as depicted in Figure 8 when CPO:MEOH molar ratio of 1:12 and lower is used, in which the feed stream consists of unreacted CPO of $\geq$69.84 wt % and MEOH of $\leq$30.16 wt %.

However, the major finding found from this study shows that controlling the phase behavior in the reaction mixture is not solely based on the CPO:MEOH molar ratio as claimed by Cao et al.[62] and Falahati and Tremblay.[61] It is also depending on the catalyst concentration used in controlling the phase behavior at the feed side of the membrane reactor besides the CPO:MEOH molar ratio at the feed stream. Table 5 depicts the TG phase conditions for reactions of using CPO:MEOH molar ratio of 1:24 with various catalyst concentrations obtained from Figure 7 in part I. As the catalyst concentration decreased as shown in Table 5, TG composition at the feed side of the membrane reactor and in Phase II increased due to the decreasing TG conversion. It is noticed from Table 5 that Phase II of the reactions that used catalyst concentrations of 0.05 and 0.1 wt % consist of 78–96 wt % of TG even TG composition in the bulk phase were following to the scale of TG $\leq$ 53.65 wt % as depicted in Figure 8. As a result, phase inversion happened at the feed side of the membrane reactor whereby TG-rich phase (Phase II) became the continuous phase and MEOH-in-TG emulsion formed as shown in Table 5. This also explains Phase II permeated through the pores of membranes to give the high TG concentration in the permeate stream in both experimental runs as shown in Figures 7c, e.

Furthermore, due to the permeation of TG-rich phase that had become continuous phase in the reactor, lower permeate fluxes were obtained for experimental reactions that used catalyst concentration of 0.05 and 0.1 wt % as shown in Figure 6 in part I. Similar observation was also reported by Cheng et al.[60] Therefore, the minimum catalyst concentration of 0.5 wt % should be used for the biodiesel production from untreated CPO in the membrane reactor to avoid phase inversion.

The results obtained in this section shows that the membrane separation efficiency is highly depending on the formation of micelle, which has been repeatedly reported by many literatures.[62–64] The formation of micelle is highly depending on the catalyst concentration and CPO:MEOH molar ratio. Therefore, the model evaluation results have successfully shown the validity of the integration of Maxwell–Stefan model with CPE model by considering the effects of CPE at the feed side of membrane reactor and the mass transport behavior at the concentration polarization layer and intramembrane layer of the membrane reactor on the final biodiesel purity.

Table 5. TG Phase Conditions for Reaction of Using CPO:MEOH Molar Ratio of 1:24 with Various Catalyst Concentrations at Steady-State Condition

NAOH Concentration (wt %)	TG Composition in Bulk Phase (wt %)	TG Composition in *Phase II* (wt %)	TG Phase Condition
0.05	42–50	80–96	Continuous phase
0.1	39–50	78–96	Continuous phase
0.5	2–15	2–20	Micelles

Conclusions

In the present article, the mathematical model of modified Maxwell–Stefan equations integrated with CPE was used for the first time to simulate the simultaneous CPE and multicomponent mass transport phenomena in the biodiesel production from CPO using the membrane reactor, which gives a good fit to the experimental data at all the conditions tested with the error values maintained within RMSD values ranges within ±5%. At the cross flow velocity of 0.75 m s^{-1}, reversible fouling with δ_{pol} ranging from 0.000086 to 0.0017 m was found to be the major fouling phenomena of the membrane reactor and complete recovery of membrane permeability by forward flushing shows that no pore plugging of solutes in the membrane. This proved the validity of the model developed with the consideration of concentration polarization layer and intramembrane phenomena. Furthermore, high and constant solute rejection, R_{app} values were obtained as the TMP increases shows that the biodiesel production process using the membrane reactor requires low energy consumption as the ultrafiltration membrane can be operated at low TMP of 103.4 kPa.

Furthermore, the experimental and simulation results show that permeate and micelles compositions were closely related to Phase I and Phase II of the CPE of transesterification system, respectively, at the feed side of the membrane reactor. For reaction of using CPO:MEOH molar ratio of 1:24 with catalyst concentration of 0.5 wt %, TG-rich phase or micelles (Phase II) were retained by the membrane and TG free permeate (Phase I) was obtained, whereas phase inversion happened when catalyst concentration of 0.05 and 0.1 wt % were used as TG-rich phase became continuous phase and permeate through the membrane. This finding shows the important of catalyst concentration and CPO:MEOH molar ratio in controlling the chemical reaction and phase behavior at the feed side of the membrane reactor, which affects the final purity of FAME in the permeate stream. This emphasized the important of incorporating the CPE model into the multicomponent mass transport of modified Maxwell–Stefan model modeling due to the close relationship between permeate compositions and feed bulk concentration in the membrane reactor. Last but not least, it is of great interest to investigate whether the application of develop model for actual process design in the industry is successful, especially for multicomponent systems, and it will be considered in our future work.

Acknowledgments

The authors thank the management of Malaysian Palm Oil Board (MPOB) for providing financial support for this study. Technical assistance by the staffs of Biodiesel Technology Group of MPOB is deeply appreciated.

Notation

A_c = cross sectional area, m^2
B_o = permeability parameter
$[B]$ = Maxwell–Stefan friction matrix
c = molar concentration, mol L^{-1}
c_{Vieth} = Vieth constant
d_i = total driving force on component i, m^{-1}
Đ = Maxwell–Stefan diffusion coefficient, m^2 s^{-1}
D_{turb} = turbulent diffusivity coefficient, m^2 s^{-1}
$Đ_{ij}^{o}$ = diffusion coefficient of solute i present in infinitely low concentration in solvent j, m^2 s^{-1}
$\bar{D}$ = average Fickian diffusive mass-transfer coefficient, m^2 s^{-1}
$[D]$ = Fickian molecular diffusion matrix
$[D]_{turb}$ = turbulence diffusivity matrix
d_{tube} = diameter of the tubular membrane, m
f = total friction force, m^{-1}
f = = Fanning friction factor
F = = molar flow rate, mol min^{-1}
F = Faraday's constant
$[F']$ = convective part matrix
g = total body force per mass of component, N kg^{-1}
g = gravitation constant, m^3 kg^{-1} s^{-2}
$[G]$ = generalized friction matrix
ΔG^o = standard free energy change, J mol^{-1}
h_f = friction head, m
$[I]$ = identity matrix
J = permeate flux, m s^{-1}
k' = effective rate constant, L mol^{-1} min^{-1}
k = mass-transfer coefficient, m s^{-1}
K = phase equilibrium ratio
K_{eq} = reaction equilibrium constants
$[K_{eq}]$ = equilibrium matrix
$[K_{eq}]_m$ = equilibrium partition coefficient
L_m = membrane thickness, m
L_p = hydraulic permeability constant
L_{tube} = length the tube, m
M_{NAOH} = molarity of standard NAOH solution, mol mL^{-1}
M_j = molar mass of the solvent, g mol^{-1}
MW = molecular weight, g mol^{-1}
n = number of moles, mol
n = number of solutes
n_{tube} = number of tubes per membrane module
N = molar flux, mol m^2 min^{-1}
P = pressure, kPa
ΔP_{total} = total pressure difference of the system or transmembrane pressure, kPa
Q = volumetric flow rate, L h^{-1}
r_{im} = friction force between component i and membrane, m^{-1}
r_{pore} = pore radius, m
R = gas constant, J K^{-1} mol^{-1}
R_{app} = apparent solute rejection
R_m = membrane resistance, m^{-1}
R_s = resistance due to solute, m^{-1}
Re = Reynolds number
Sc = Schmidt number
Sc_{turb} = turbulence Schmidt number
Sh = Sherwood number
t = time, min
T = temperature, K
u = specific velocity, m s^{-1}
u_t = bulk flow velocity/cross flow velocity, m s^{-1}
u^v = volume-averaged velocity (or volumetric flux), m^3 s^{-1} m^{-2}
v = kinematic viscosity, m^2 s^{-1}
v_{turb} = turbulent kinematic viscosity, m^2 s^{-1}
V_i = molar volume of solute i at its normal boiling temperature, m^3 mol^{-1}
$\dot{V}_{out}$ = volumetric flow rate of the permeate, L min^{-1}
ΔV = differential volume, L
$\bar{V}$ = specific molar volume, m^3 $kmol^{-1}$
W = unit weights
x = mole fraction
X = Phase II
y^+ = dimensionless distance coordinate in the polarization layer
Y = Phase I
z = distance coordinate perpendicular to the membrane surface, m
Z = number of charges

Greek letters

γ = activity coefficient
$\bar{\gamma}$ = average activity coefficient
σ = osmostic reflection coefficient
η = Viscosity, kg m^{-1} s^{-1}
η = dynamic viscosity, Pa s
η_m = dynamic viscosity of mixture, Pa s
Φ = average segment fraction
Φ = electrical potential
Φ_j = association factor for the solvent j
θ = average area fraction

δ_{ij} = Kronecker delta
δ_{pol} = thickness of boundary layer, m
μ = chemical potential, J mol^{-1}
κ = fractional viscosity coefficient, s^{-1}
ε = error
ε = membrane porosity
τ = empirical parameter
τ = membrane tortuosity
τ = residence time, h
α_m = membrane resistance factor, m^{-2}
ξ = interaction parameter
β = stoichiometric coefficient
ω = mass fraction
$[\Gamma_c]$ = thermodynamic correction factor matrix
$\Delta\Pi$ = osmostic pressure difference across the membrane, kPa

Subscripts

b = bulk phase
calc = calculated value
CPO = crude palm oil
exp = experimental value
F = feed
guess = guess value
in = inlet to the reactor
i, j, k = individual component/solute
m = membrane
max = maximum
MEOH = methanol
MEOH/NAOH = solvent of methanol and sodium hydroxide
o = initial
out = outlet/permeate from the reactor
p = permeate
pol = polarization layer
r = retentate
t = total
tube = tubular membrane

Superscripts

I = *Phase I*
II = *Phase II*
m = membrane
$'$ = membrane interface

Abbreviation

CPE = chemical and phase equilibrium
CPO = crude palm oil
DG = diglyceride
FAME = fatty acid methyl ester
GLY = glycerol/glycerine
LHS = left-hand side
LLE = liquid–liquid equilibrium
MEOH = methanol
MG = monoglyceride
MPOB = Malaysian palm oil board
RHS = right-hand side
TG = triglyceride
TMP = transmembrane pressure
UF = ultrafiltration
UNIQUAC = UNIversal QUAsiChemical

Literature Cited

1. Kerkhof PJAM. A modified Maxwell-Stefan model for transport through inert membranes: the binary friction model. *Chem Eng J Biochem Eng J*. 1996;64(3):319–343.
2. Sanderson RV, Chien HHY. Simultaneous chemical and phase equilibrium calculation. *Ind Eng Chem Process Des Dev*. 1973;12(1):81–85.
3. Rajca M, Bodzek M, Konieczny K. Application of mathematical models to the calculation of ultrafiltration flux in water treatment. *Desalination*. 2009;238(1–3):100–110.
4. Van Oers CW, Vorstman MAG, Hout RVD, Kerkhof PJAM. The influence of thermodynamic activity on the solute rejection in multicomponent systems. *J Membr Sci*. 1997;136(1–2):71–87.
5. Ahmad AL, Chong MF, Bhatia S. Mathematical modeling and simulation of the multiple solutes system for nanofiltration process. *J Membr Sci*. 2005;253(1–2):103–115.
6. Binning R, Lee R, Jennings J, Martin E. Separation of liquid mixtures by permeation. *Ind Eng Chem*. 1961;53(1):45–50.
7. Wijmans JG, Baker RW. The solution-diffusion model: a review. *J Membr Sci*. 1995;107(1–2):1–21.
8. Tessendorf S, Gani R, Michelsen ML. Modeling, simulation and optimization of membrane-based gas separation systems. *Chem Eng Sci*. 1999;54(7):943–955.
9. Coker DT, Freeman BD, Fleming GK. Modeling multicomponent gas separation using hollow-fiber membrane contactors. *AIChE J*. 1998;44(6):1289–1300.
10. Krovvidi KR, Kovvali AS, Vemury S, Khan AA. Approximate solutions for gas permeators separating binary mixtures. *J Membr Sci*. 1992;66(2–3):103–118.
11. Qi R, Henson MA. Modeling of spiral-wound permeators for multicomponent gas separations. *Ind Eng Chem Res*. 1997;36(6):2320–2331.
12. Thundyil MJ, Koros WJ. Mathematical modeling of gas separation permeators - for radial crossflow, countercurrent, and cocurrent hollow fiber membrane modules. *J Membr Sci*. 1997;125(2):275–291.
13. Sloot HJ, Smolders CA, Van Swaaij WPM, Versteeg GF. High-temperature membrane reactor for catalytic gas-solid reactions. *AIChE J*. 1992;38:887–900.
14. Tu S-C, Ravindran V, Den W, Pirbazari M. Predictive membrane transport model for nanofiltration processes in water treatment. *AIChE J*. 2001;47(6):1346–1362.
15. Chellam S, Wiesner MR. Particle transport in clean membrane filters in laminar flow. *Environ Sci Technol*. 1992;26(8):1611–1621.
16. Chellam S, Wiesner MR. Particle back-transport and permeate flux behavior in crossflow membrane filters. *Environ Sci Technol*. 1997;31(3):819–824.
17. van den Berg GB, Smolders CA. Flux decline in membrane processes. *Filtr Sep*. 1988;25(2):115–121.
18. Pirbazari M, Badriyha BN, Ravindran V. MF-PAC for treating waters contaminated with natural and synthetic organics. *J Am Water Works Assoc*. 1992;84(12):95–103.
19. Ghaffour N. Modeling of fouling phenomena in cross-flow ultrafiltration of suspensions containing suspended solids and oil droplets. *Desalination*. 2004;167:281–291.
20. Damak K, Ayadi A, Zeghmati B, Schmitz P. A new Navier-Stokes and Darcy's law combined model for fluid flow in crossflow filtration tubular membranes. *Desalination*. 2004;161(1):67–77.
21. Tansel B, Bao WY, Tansel IN. Characterization of fouling kinetics in ultrafiltration systems by resistances in series model. *Desalination*. 2000;129(1):7–14.
22. Katsikaris K, Boukouvalas C, Magoulas K. Simulation of ultrafiltration process and application to pilot tests. *Desalination*. 2005;171(1):1–11.
23. Wijmans JG, Nakao S, Smolders CA. Flux limitation in ultrafiltration: osmotic pressure model and gel layer model. *J Membr Sci*. 1984;20(2):115–124.
24. Ko MK, Pellegrino JJ. Determination of osmotic pressure and fouling resistance and their effects of performance of ultrafiltration membranes. *J Membr Sci*. 1992;74(1–2):141–157.
25. Abejón R, Garea A, Irabien A. Integrated countercurrent reverse osmosis cascades for hydrogen peroxide ultrapurification. *Comput Chem Eng*. 2012;41:67–76.
26. Ciora RJ Jr, Liu PKT. Ceramic membranes for environmental related applications. *Fluid Part Sep J*. 2003;15(1):51–60.
27. Prakash Rao A, Desai NV, Rangarajan R. Inorganic membranes: new materials for separation technology. *J Sci Ind Res*. 1997;56(9):518–522.
28. Kabsch-Korbutowicz M, Urbanowska A. Water treatment in integrated process using ceramic membranes. *Pol J Environ Stud*. 2010;19(4):731–737.
29. Zakrzewska-Trznadel G. Radioactive waste processing: advancement in pressure-driven processes and current world scenario. In: Pabby AK, Rizvi SSH, Sastre AM, editors. *Handbook of Membrane Separations: Chemical, Pharmaceutical, Food, and Biotechnological Applications*. London: CRC Press, Taylor & Francis Group, 2009:844.
30. Allgeier S, Alspach B, Vickers J. *Membrane Filtration Guidance Manual*. 2005. Available at: http://www.epa.gov/safewater/lt2/guides.html.
31. Oh PP. Modelling of a membrane reactor system for crude palm oil transesterification. Doctoral Dissertation. University of Nottingham Malaysia Campus, United States, 2014.
32. Chong MF, Chen J, Oh PP, Chen Z-S. Modeling study of chemical phase equilibrium of canola oil transesterification in a CSTR. *Chem Eng Sci*. 2013;87:371–380.

33. Wesselingh JA, Krishna R. *Mass Transfer in Multicomponent Mixtures*. Malaysia: Delft University Press, 2000.
34. Lightfoot EN. *Transport Phenomena and Living Systems: Biomedical Aspects of Momentum and Mass Transport*. New York: Wiley, 1974.
35. Standart GL, Taylor R, Krishna R. The Maxwell-Stefan formulation of irreversible thermodynamics for simultaneous heat and mass transfer. *Chem Eng Commun*. 1979;3(4–5):277–289.
36. Taylor R, Krishna R. *Multicomponent Mass Transfer*. New York: Wiley, 1993.
37. Wilke CR. A viscosity equation for gas mixture. *J Chem Phys*. 1950;18(4):517–520.
38. Krishna R. A simplified procedure for the solution of the dusty gas model equations for steady-state transport in non-reacting systems. *Chem Eng J*. 1987;35(2):75–81.
39. Anderson JL, Malone DM. Mechanism of osmotic flow in porous membranes. *Biophys J*. 1974;14(12):957–982.
40. Wilke CR, Chang P. Correlation of diffusion coefficients in dilute solutions. *AIChE J*. 1955;1(2):264–270.
41. Bowen WR, Jenner F. Theoretical descriptions of membrane filtration of colloids and fine particles: an assessment and review. *Adv Colloid Interface Sci*. 1995;56:141–200.
42. Gando-Ferreira LM, Brito P, Portugal A, Blox M, Kerkhof P. A simulation study on the transport phenomena in ultrafiltration. In: *Workshop on Modelling and Simulation in Chemical Engineering*. Coimbra, Portugal, 2003.
43. Stewart WE. Multicomponent mass transfer in turbulent flow. *AIChE J*. 1973;19(2):398–400.
44. Toor HL. Turbulent diffusion and the multicomponent reynolds analogy. *AIChE J*. 1960;6(3):525–527.
45. Karode SK. Unsteady state flux response: a method to determine the nature of the solute and gel layer in membrane filtration. *J Membr Sci*. 2001;188(1):9–20.
46. Jonsson G. Boundary layer phenomena during ultrafiltration of dextran and whey protein solutions. *Desalination*. 1984;51(1):61–77.
47. Brito P, Gando-Ferreira LM, Portugal A. Simulation of membrane separations using a modified Maxwell-Stefan model. In: *10th International Chemical and Biological Engineering Conference*. Braga, Portugal, 2008.
48. Krishna R, Standart GL. A multicomponent film model incorporating a general matrix method of solution to the Maxwell-Stefan equations. *AIChE J*. 1976;22(2):383–389.
49. Kimura S. Analysis of reverse osmosis membrane behaviors in a long-term verification test. *Desalination*. 1995;100(1–3):77–84.
50. Wijmans JG, Nakao S, Van Den Berg JWA, Troelstra FR, Smolders CA. Hydrodynamic resistance of concentration polarization boundary layers in ultrafiltration. *J Membr Sci*. 1985;22(1):117–135.
51. Sarbolouki MN, Miller IF. On pore flow models for reverse osmosis desalination. *Desalination*. 1973;12(3):343–359.
52. Poling BE, Prausnitz JM, O'Connell JP. *The Properties of Gases and Liquids*, 5th ed. Amsterdam; New York: The McGraw-Hill Companies, Inc., 2001.
53. Mehta A, Zydney AL. Permeability and selectivity analysis for ultrafiltration membranes. *J Membr Sci*. 2005;249(1–2):245–249.
54. Ahmad AL, Chong MF, Bhatia S. Ultrafiltration modeling of multiple solutes system for continuous cross-flow process. *Chem Eng Sci*. 2006;61(15):5057–5069.
55. Viswanath D, Ghosh T, Prasad DL, Dutt NK, Rani K. *Correlations and estimation of pure liquid viscosity. Viscosity of Liquids*. The Netherlands: Springer, 2007:135–405.
56. Nobel PS. 3 - Solutes. In: Nobel PS, editor. *Physicochemical and Environmental Plant Physiology*, *3rd ed*. Burlington: Academic Press, 2005:99–170.
57. Portha JF, Allain F, Coupard V, Dandeu A, Girot E, Schaer E, Falk L. Simulation and kinetic study of transesterification of triolein to biodiesel using modular reactors. *Chem Eng J*. 2012;207–208:285–298.
58. Stamenković OS, Veljković VB, Todorović ZB, Lazić ML, Banković-Ilić IB, Skala DU. Modeling the kinetics of calcium hydroxide catalyzed methanolysis of sunflower oil. *Bioresour Technol*. 2010;101(12):4423–4430.
59. Mostinsky IL, Diffusion coefficient. *Thermopedia*. 2011. Available at http://www.thermopedia.com/content/696/. Accessed on October 13, 2014.
60. Cheng L-H, Cheng Y-F, Yen S-Y, Chen J. Ultrafiltration of triglyceride from biodiesel using the phase diagram of oil–FAME–MeOH. *J Membr Sci*. 2009;330(1–2):156–165.
61. Falahati H, Tremblay AY. The effect of flux and residence time in the production of biodiesel from various feedstocks using a membrane reactor. *Fuel*. 2012;91(1):126–133.
62. Cao P, Tremblay AY, Dubé MA, Morse K. Effect of membrane pore size on the performance of a membrane reactor for biodiesel production. *Ind Eng Chem Res*. 2007;46(1):52–58.
63. Cao P, Tremblay AY, Dube´ MA. Kinetics of canola oil transesterification in a membrane reactor. *Ind Eng Chem Res*. 2009;48(5):2533–2541.
64. Dubé MA, Tremblay AY, Liu J. Biodiesel production using a membrane reactor. *Bioresour Technol*. 2007;98(3):639–647.

Appendix : Derivation of the Flux Equations for the Binary Friction Maxwell–Stefan Model

Multiplying Eq. 5 with c_t, it becomes

$$\sum_{\substack{j=1\\ j\neq i}}^{n}\frac{x_iN_j-x_jN_i}{\text{Đ}_{ij}}-c_t\frac{1}{B_o}\kappa_i\phi_iu_i=c_t\frac{x_j}{RT}\nabla_{T,P}\mu_i+\frac{\phi_i}{RT}\nabla\text{P} \tag{A1}$$

The first term on the RHS of A1, we can write[1,36]

$$\frac{c_tx_i}{RT}\nabla_{T,P}\mu_i=c_t\sum_{j=1}^{n-1}\Gamma_{\text{ij}}\nabla x_j \tag{A2}$$

The second term on the RHS of A1 can be written as[1]

$$\begin{aligned}\frac{\phi_i}{RT}\nabla P &=c_i\frac{\bar{V}_i}{RT}\nabla P\\ &=-\frac{c_i\bar{V}_i}{RT}\left(\frac{c_tRT}{B_o}\sum_{j=1}^{n}\kappa_j\phi_ju_j\right)\\ &=-\frac{c_i\bar{V}_ic_t}{B_o}\sum_{j=1}^{n}\kappa_jN_j\bar{V}_j\\ &=-\frac{c_i\bar{V}_ic_t}{B_o}\left(\sum_{j=1}^{n-1}\kappa_jN_j\bar{V}_j+\kappa_nN_n\bar{V}_n\right)\\ &=-\frac{c_i\bar{V}_ic_t}{B_o}\left(\sum_{j=1}^{n-1}\kappa_jN_j\bar{V}_j+\kappa_n\bar{V}_n\left(N_t-\sum_{j=1}^{n-1}N_j\right)\right)\\ &=-\frac{c_i\bar{V}_ic_t}{B_o}\left(\sum_{j=1}^{n-1}N_j\left(\kappa_j\bar{V}_j-\kappa_n\bar{V}_n\right)+\kappa_nN_t\bar{V}_n\right)\end{aligned} \tag{A3}$$

The Maxwell–Stefan diffusion term is defined as[36]

$$\sum_{\substack{j=1\\ j\neq i}}^{n}\frac{x_iN_j-x_jN_i}{\text{Đ}_{ij}}=\frac{N_tx_i}{\text{Đ}_{\text{in}}}+x_i\sum_{j=1}^{n-1}N_j\left(\frac{1}{\text{Đ}_{ij}}-\frac{1}{\text{Đ}_{in}}\right)-N_i\sum_{k=1}^{n}\frac{x_k}{\text{Đ}_{ik}} \tag{A4}$$

The second term on the LHS of A1 can be written as[1]

$$\begin{aligned}c_t\frac{1}{B_o}\kappa_i\phi_iu_i &=\frac{c_t}{B_o}\kappa_i(c_i\bar{V}_i)\left(\frac{N_i}{c_i}\right)\\ &=\frac{c_t}{B_o}\kappa_i\bar{V}_iN_i\end{aligned} \tag{A5}$$

Substituting A2, A3, A4, and A5 into A1, resulting in

$$\begin{aligned}&\frac{N_tx_i}{\text{Đ}_{\text{in}}}+x_i\sum_{j=1}^{n-1}N_j\left(\frac{1}{\text{Đ}_{ij}}-\frac{1}{\text{Đ}_{\text{in}}}\right)-N_i\sum_{k=1}^{n}\frac{x_k}{\text{Đ}_{ik}}-\frac{c_t}{B_o}\kappa_i\bar{V}_iN_i\\ &\quad=c_t\sum_{j=1}^{n-1}\Gamma_{\text{ij}}\nabla x_j-\frac{c_i\bar{V}_ic_t}{B_o}\left(\sum_{j=1}^{n-1}N_j\left(\kappa_j\bar{V}_j-\kappa_n\bar{V}_n\right)+\kappa_nN_t\bar{V}_n\right)\end{aligned} \tag{A6}$$

Rearranging A6, we obtained

$$c_t \sum_{j=1}^{n-1} \Gamma_{ij} \nabla x_j - \frac{N_t x_i}{\mathfrak{D}_{in}} - \frac{N_t x_i c_t^2 \bar{V}_i \bar{V}_n}{B_o} \kappa_n = \frac{x_i c_t^2 \bar{V}_i}{B_o} \sum_{j=1}^{n-1} N_j \left(\kappa_j \bar{V}_j - \kappa_n \bar{V}_n\right) + x_i \sum_{j=1}^{n-1} N_j \left(\frac{1}{\mathfrak{D}_{ij}} - \frac{1}{\mathfrak{D}_{in}}\right) - N_i \sum_{k=1}^{n} \frac{x_k}{\mathfrak{D}_{ik}} - \frac{c_t}{B_o} \kappa_i \bar{V}_i N_i \tag{A7}$$

and further arranging it into

$$c_t \sum_{j=1}^{n-1} \Gamma_{ij} \nabla x_j - N_t x_i \left(\frac{1}{\mathfrak{D}_{in}} + \frac{c_t^2 \bar{V}_i \bar{V}_n}{B_o} \kappa_n\right) = \frac{x_i c_t^2 \bar{V}_i}{B_o} \sum_{j=1}^{n-1} N_j \left(\kappa_j \bar{V}_j - \kappa_n \bar{V}_n\right) + x_i \sum_{j=1}^{n-1} N_j \left(\frac{1}{\mathfrak{D}_{ij}} - \frac{1}{\mathfrak{D}_{in}}\right) - N_i \sum_{k=1}^{n} \frac{x_k}{\mathfrak{D}_{ik}} - \frac{c_t}{B_o} \kappa_i \bar{V}_i N_i \tag{A8}$$

Table A1. Terms for Friction Matrixes and Thermodynamic Factor Matrix

Term	Term from A8
$[G]_{ij}$	$[B]_{ij}$ and the first and forth terms on the RHS of A8
$[B]_{ii}$	The third term on the RHS of A8
$[B]_{ij}$	The second term on the RHS of A8
$[F]_{ij}$	The second term on the LHS of A8
$[\Gamma]_{ij}$	The first term on the LHS of A8

From A8, the friction matrixes and thermodynamic factor matrix are obtained as as shown in Table A1. Equations 8 and 11 are then obtained by multiplying $[G]_{ij}$ and $[F]_{ij}$ with $\frac{\tau}{\varepsilon}$. And, Eqs. 9, 10, and 12 are formed by the term $[B]_{ii}$, $[B]_{ij}$, and $[\Gamma]_{ij}$ as shown in Table A1.

Manuscript received July 10, 2014, and revision received Jan. 7, 2015.